Molecular Physics, Vol. 105, Nos. 2–3, 20 January–10 February 2007, 147–156

Atomic scale design of nanostructures

J. BERNHOLC*†‡, W. LU†, S. M. NAKHMANSON§, P.H. HAHN†¶, V. MEUNIER‡, M. BUONGIORNO NARDELLI†‡ and W.G. SCHMIDT†‖

†Center for High Performance Simulation and Department of Physics, NC State University, Raleigh, NC 27695-7518, USA

‡Computer Science and Mathematics Division, Oak Ridge National Laboratory, Oak Ridge, TN 37831-6367, USA

§Department of Physics and Astronomy, Rutgers University, Piscataway, NJ 08854, USA

¶Institut für Festkörpertheorie und-optik, Friedrich-Schiller-Universität, Max-Wien-Platz 1, 07743 Jena, Germany

‖Theoretische Physik, Universität Paderborn, 33095 Paderborn, Germany

(*Received 15 June 2006; in final form 17 December 2006*)

Recent advances in theoretical methods and high performance computing allow for reliable first-principles predictions of complex nanostructured materials and devices. This paper describes three examples: (i) non-equilibrium electron transport through molecular junctions, as a stepping stone for the design of molecular-scale devices and for integration of biomolecules with Si technology; (ii) polarization and piezoelectric properties of PVDF and related polymers; and (iii) the many-body optical spectrum of water. For the molecular junction, our results provide a qualitative picture and quantitative understanding of the mechanism leading to negative differential resistance for a large class of small molecules. For ferroelectric polymers, the calculations show that their polarization is described by cooperative, quantum-mechanical interactions between polymer chains. Nevertheless, the *ab initio* results lead to a simple parameterization of polarization as a function of copolymer concentration. Finally, our calculations explain the well-known redshift in the fundamental absorption of water as due to exciton delocalization upon aggregation.

1. Introduction

We describe three applications of our large-scale *ab initio* methodology: (i) an investigation of the properties of molecular junctions compatible with Si-based electronics; (ii) a comprehensive study of polarization in ferroelectric polymers in the PVDF family; and (iii) a many-body investigation of the optical spectrum of water.

Electron transport through molecular-scale devices has attracted considerable attention among both experimentalists and theorists. Most studies of these systems have focused on molecules connected to metallic leads.

Recently, several experimental and theoretical investigations of the transport properties of various organic molecules on Si surfaces have been reported [1–3]. These systems have a number of advantages compared to the traditional molecule–metal junctions. First, the organic molecules can be patterned on the Si surface [4, 5], because of the thermodynamic and kinetic stability of the Si–C bond. Second, the bonding between organic molecules and Si surface atoms is well understood [4–7], which should allow for straightforward comparisons between theoretical and experimental results on exactly the same atomic configuration. Third, there is a tremendous potential for applications combining Si microelectronics with organics-based structures, e.g. porphyrins on Si(001) are promising candidates for molecular memories [8]. As a paradigmatic example, we investigate the transport properties of 1,4-diethynylbenzene connected between two hydrogenated Si(111) surface fragments. In this paradigmatic geometry, the bonding to Si is well defined [4, 5], thereby avoiding the ambiguity of the contact geometry of metal-connected molecules.

Ferroelectric materials are critically important for a wide range of current and prospective technological applications. These are not limited to various electromechanical devices, like sensors, actuators and

*Corresponding author. Email: bernholc@ncsu.edu

Molecular Physics
ISSN 0026–8976 print/ISSN 1362–3028 online © 2007 Taylor & Francis
http://www.tandf.co.uk/journals
DOI: 10.1080/00268970701189186

transducers, but also include nonvolatile ferroelectric memories, high-k dielectrics for modern microelectronics, pyroelectric arrays, and acoustic and nonlinear optical devices. Unfortunately, however, there exist only very few classes of materials that exhibit ferroelectric behaviour. Perovskite-type ABO_3 metal oxides (e.g. $BaTiO_3$ or $KNbO_3$), comprising the most important class of ferroelectric materials, are widely known for their strong polarization and excellent piezoelectric response. Still, their usefulness is limited by heavy weight, brittleness and substantial costs of device manufacturing. Ferroelectric polymers, on the other hand, exhibit properties almost *complementary* to those of perovskite-type oxides. In addition to being respectable piezo- and pyroelectrics, they are light, flexible and nontoxic [9–14], which is particularly important in the view of the recent interest in new, more efficient and environmentally friendly materials.

Polyvinylidene fluoride (PVDF), $[–CH_2–CF_2–]_n$, the most well-known ferroelectric polymer, is a complex material that is usually synthesized as a mixture of ordered and disordered phases, and requires some postprocessing in the form of stretching and poling to become ferroelectric. Since, even after the aforementioned postprocessing procedure, β-PVDF is manufactured at best only 50% crystalline, until very recently there had been no certainty about the value of polarization in the fully crystalline material. The various models do not agree with each other, which recently motivated us to apply modern *ab initio* techniques to compute spontaneous polarization in β-PVDF [15]. Our results clearly show that the majority of the previous models, fitted either to experiment or to a simple sum of the bond-dipole moments in an *individual* VDF monomer [11, 14] ($\simeq$2 Debyes), underestimate the strength of the dipole–dipole interaction in this material.

Moreover, although the ideal β-PVDF structure serves well as a simple model for basic understanding of the polar nature of ferroelectric polymer crystals, it is quite different from the polymeric structures used in actual device manufacturing. Since poor crystallinity of 'pure' PVDF degrades its polar properties, it is usually mixed with tri-fluoroethylene (TrFE), $[–CHF–CF_2–]$, and tetra-fluoroethylene (TeFE), $[–CF_2–CF_2–]$ to produce device-grade materials. Naturally, compared to VDF, TrFE and TeFE monomers exhibit lower or no polarization. However, such P(VDF/copolymer) systems can be grown with 90% or better crystallinity [10, 16–18], which results in stronger polarization and piezoelectric response than that of 50% crystalline PVDF. However, it turns out that realistic *ab initio* models of polarization in these materials are required to explain the peculiarities of their behaviour and to open avenues for development of better polymeric ferroelectrics for modern technological applications.

The optical spectrum of water provides an important signature for its detection and a measure of its properties. However, its absorption spectrum was not well understood, despite decades of effort. The optical spectra of amorphous, hexagonal as well as cubic ice are dominated by a very pronounced first absorption peak at about 8.7 eV [19, 20], while the absorption spectrum of the liquid shows a similar structure [21, 22]. In the case of cubic ice, the first absorption peak was directly related to the calculated density of states [23]. Nevertheless, the universal occurrence of the 8.7 eV peak in a variety of water phases suggests its molecular origin, as opposed to being due to specific transitions between electronic states arising from a crystalline structure with a particular symmetry. However, the lowest-lying excitation of the H_2O molecule occurs at 7.4 eV [24]. Intermolecular interactions are expected to induce a significant broadening of the energy levels relative to the isolated molecule. This should lead to a decrease of the transition energies relative to the molecular values [25–27]. Numerical studies of the optical properties of ice [28] based on the local density approximation, i.e. neglecting many-body effects beyond a mean-field description, indeed find the absorption onset at just below 6 eV.

The blueshift observed experimentally upon condensation of water molecules has been alternatively attributed to excitons of *molecular* origin [26, 27] or to solvation and Rydbergization effects (destabilization of highly excited states in condensed phases by interactions with nearby molecules) [29]. However, accurate description of optical spectra requires inclusion of many-body correlation effects from *first principles*, which is a difficult and computationally expensive task for complex disordered systems, such as water or the structurally disordered forms of ice.

We exploit the recent progress in accurate modelling of optical properties using the many-body Green's function approach [30] to explain and quantitatively account for the peculiar absorption properties of solid water and H_2O molecules. The results highlight the major role played by nearby hydrogen-bonded water molecules in affecting the spacial extent and the energetics of the exciton dominating the major absorption peak. It is clear that the exciton state 'sees' nearby molecules due to its spacial extent and that its energetics will be affected by changes in the first and even the second coordination shell. Variations in the first absorption peak may thus be used to uncover microscopic aspects of solvation.

2. Methodology

Most of the calculations were performed using our *ab initio* multigrid-based total-energy method, employing a real-space grid as a basis [31]. The electron–ion interactions were represented by nonlocal, norm-conserving pseudopotentials.

In calculating the I/V characteristics, we used the non-equilibrium Green's function (NEGF) method [32, 33] in a basis of optimally localized orbitals [34, 35]. For polarization calculations,we employed the Wannier function formalism [36, 37], which provides a particularly transparent avenue for evaluating the contributions of the various parts of the system.

For calculating the optical spectrum of water, we proceed in three steps: (i) we use density-functional theory in the generalized gradient approximation (DFT-GGA) to obtain the structurally relaxed ground state configuration of ice-Ih and the Kohn–Sham eigenvalues and eigenfunctions that enter the single- and two-particle Green's functions, (ii) the electronic quasiparticle spectrum is obtained within the GW approximation (GWA) [38] to the exchange-correlation self-energy, and (iii) the Bethe–Salpeter equation (BSE) is solved for coupled electron–hole excitations [39–41], thereby accounting for the screened electron–hole attraction and the unscreened electron–hole exchange [42, 43]. Additional description of the calculations is given in [44].

3. Quantum transport in Si–organic molecule–Si

The atomic configuration of the 1,4-diethynylbenzene molecule on Si(111), optimized by total energy calculations, is shown in figure 1. One molecule per (4×3) unit cell is connected to the Si(111) surfaces through a single Si–C bond, which is covalent with a typical bond length of 1.82 Å. The remaining dangling bonds of the Si surface are saturated by hydrogen atoms.

Two different ballistic transport calculations are performed with the applied bias, with and without self-consistent iterations. In both cases, the charge density in the leads is fixed and the electrostatic potentials are shifted to match their chemical potentials. For the active region, the initial charge density is chosen from the zero-bias DFT calculation and a linear potential drop across the conductor region is added to the electrostatic potential. In the non-SCF (non-self-consistent-field) calculations, the Hamiltonian matrix and the transmission coefficients are evaluated from the initial potentials. In the self-consistent calculations, the charge density and the potentials in the conductor region are determined iteratively, with the transmission coefficients obtained using the relaxed potentials and the updated matrix elements.

The I–V curves are calculated by integrating the transmission in the bias windows. They are shown in figure 2(b). From figure 2(b), it is clear that when the bias is smaller than 1.4 V, the non-SCF calculations result in very similar I–V characteristics to those of

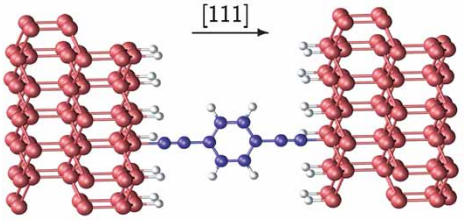

Figure 1. Optimized geometry of the Si(111) – 1,4-diethynylbenzene–Si(111) junction. The large, medium and small balls represent Si, C and H atoms, respectively. The molecules are arranged periodically on the (111) surface with one molecule per (4×3) unit cell. Semi-infinite Si(111) on both sides of the molecule mimic the presence of the leads.

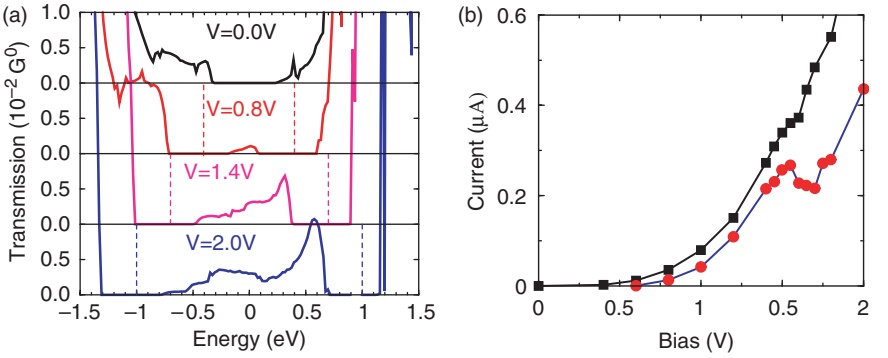

Figure 2. (a) Self-consistent transmission coefficients through 1,4-diethynylbenzene connected to hydrogenated Si(111) leads. Bias windows are shown as dashed lines. The energy zeros are chosen to be at the centre of each bias window. (b) I–V curve for 1,4-diethynylbenzene between Si(111) leads. The squares and circles represent results from non-self-consistent and self-consistent calculations, respectively. The lines are just a guide to the eye.

SCF calculations. In this bias region, the current exponentially increases with the applied bias, as expected for a system with a gap. However, when the bias is larger than 1.5 V, self-consistency becomes very important. A very small shoulder appears at 1.6 V in the non-SCF calculation, while a current valley, i.e. a negative differential resistance, is observed in SCF calculations. This underlines the importance of performing fully self-consistent calculations at large biases, when the device is far from equilibrium.

In order to understand the mechanism of electron transport through the molecule, we calculated the position-dependent density-of-states in the active region. The density of states was averaged in the plane perpendicular to the current flow and colour coded, with blue and red regions corresponding to low and high electron densities, respectively. The results for the biases of 0.0, 0.8, 1.4 and 2.0 V are displayed in figure 3. The positions of molecular orbitals for the isolated molecule are also shown for comparison. The chemical potential at the right lead is chosen as the reference energy, which is different from figure 2(a).

Figure 3 clearly demonstrates the rearrangement of molecular levels with the applied bias. After the molecule is attached to the Si(111) leads and before any bias is applied, the gap between the HOMO (highest occupied molecular orbital) and the LUMO (lowest unoccupied molecular orbital) is reduced to about 2.8 eV, a 0.2 eV decrease compared to the isolated molecule. This is because the levels broaden slightly and the C–H bond at each end of the molecule is replaced by a C–Si bond. When the bias potential is increased, the levels become increasingly broader and their centres shift up relative to the chemical potential of the right lead. At a bias of about 1.4–1.5 V, the centre of the LUMO reaches the conduction band edge of the left lead and a first peak in current is observed. With a further increase of the bias, the centre of the LUMO falls into the band gap, weakening the hybridization between the LUMO and the lead states. Correspondingly, the current decreases as the bias increases, marking the onset of NDR. For biases larger than 1.7 V, the current increases again due to the following factors: first, the broadened HOMO shifts and reaches the valence band edge of the right lead, resulting in the first peak in the transmission coefficient (at -0.3 eV in figure 2(a) for $V = 2.0$ V). Second, the overlap between the LUMO and the valence band edge of the left lead contributes to another peak in the transmission coefficient (at 0.5 eV in figure 2(a) for $V = 2.0$ V). Clearly, the existence of valence and conduction band edges at both sides of the molecule results in bias-induced changes in electron transmission probabilities at each side of the molecule, and thus a complex, bias-dependent shape of the transmission function. Nevertheless, negative differential resistance at one or more bias voltages is still to be expected, as the broadened molecular levels shift with the applied voltage.

Summarizing these results, we have investigated quantum transport properties of a Si–molecule–Si system from first principles. Our results highlight the importance of self-consistent screening at large bias and the complex interplay between enhanced broadening of molecular levels and their rearrangement with respect to semiconductor band edges at both sides of the molecule. In the present system, resonant tunnelling occurs when the LUMO matches the conduction band edge of the negative lead, resulting in diminished coupling and in negative differential resistance when this orbital drops below the band edge. As the bias is further increased, resonant tunnelling occurs between the broadened HOMO and the valence band edge of the positive lead, resulting in a significant increase in transmission.

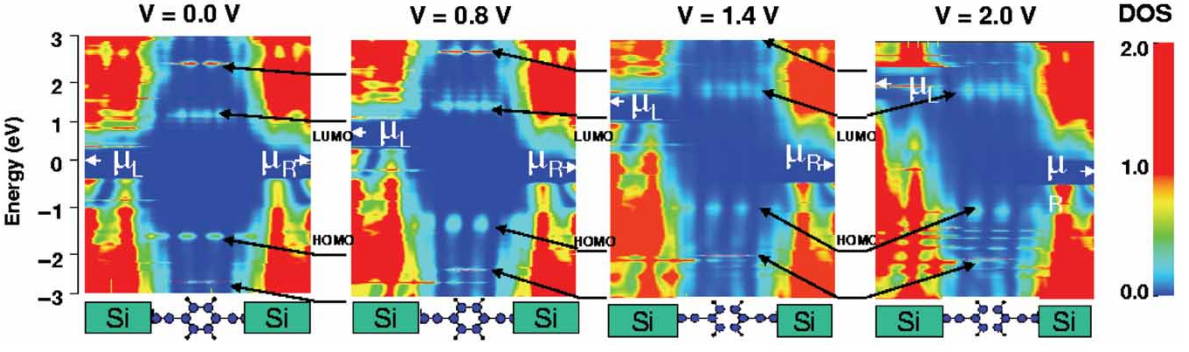

Figure 3. Position dependent density of states at biases of 0.0, 0.8, 1.4 and 2.0 V. The DOS is averaged in the plane perpendicular to the current. The orbital levels of an isolated molecule are also shown for comparison. The μ_L and μ_R are the chemical potentials for the left and the right Si leads. The blue and red colours represent regions of low and high density of states, respectively.

4. Ferroelectric polymers in the PVDF family

In order to fully understand the physics of polarization in crystalline β-PVDF and in P(VDF/copolymer) systems one needs to answer the following questions. (a) What are the main 'building blocks' governing the polar properties of a polymer–ferroelectric crystal: are these individual monomers, chains or, possibly, something else? (b) What is the 'natural value' of a structural unit dipole moment in a given environment (individual molecule, chain, crystal)? (c) What happens to this value when the environment changes, e.g. when the VDF-to-copolymer concentration changes?

In order to answer the first question, we computed average dipole moments of VDF, TrFE and TeFE structural units in finite H–$[CH_2–CF_2]_n$–H, H–$[CHF–CF_2]_n$–H and H–$[CF_2–CF_2]_n$–H polymer chains for $n = 1, \ldots, 8$. The chains were relaxed to ionic forces of less than $0.025\,\text{eV}\,\text{Å}^{-1}$ in large supercells, so that the distance between each chain and its periodic images was approximately 10 Å. In addition, we computed the same dipole moments for the limiting case of infinite chains in supercells containing four or eight structural units. The calculations were performed at both β-PVDF (2.56 Å per structural unit) and the fully relaxed lattice constants c along the chain-backbone direction. The results are presented in table 1. Our value of the VDF dipole moment is in excellent agreement with results in the literature [14, 45].

Similar results are obtained for polymer chains where one or more monomers are substituted by copolymers. The results of such calculations were obtained for the chains where one of the eight units in the supercell was substituted by TrFE, TeFE or an inverted VDF, also known as the head-to-head, tail-to-tail (HHTT) defect. All of these cases demonstrate that an introduction of an isolated defect, even as drastic as HHTT, into a β-PVDF chain does not seriously affect the polar states of the other units in the chain, except maybe the nearest neighbours of the substituted unit. On the other hand, a copolymer unit or a HHTT defect substituted into the chain keeps its own characteristic features fairly intact or even amplifies them. For example, a TrFE unit embedded into the chain has the same D_3 component as in a PTrFE chain and it also retains its large D_1 component. Similarly, the HHTT defect has its D_3 component increased to nearly 3 Debye.

Table 1. Average monomer dipole moments in the infinite PVDF, PTrFE and PTeFE chains. Values computed at β-PVDF chain-backbone lattice constant (2.56Å/unit) as well as at the relaxed lattice constant are shown.

	D_3, $c = 2.56$ Å/unit (Debye)	D_3, relaxed c (Debye)	Relaxed c (Å/unit)
VDF	2.00	2.00	2.560
TrFE	0.78	0.75	2.667
TeFE	Nonpolar	Nonpolar	2.749

We can conclude that: (i) in general, individual monomers in infinite isolated chains prefer to 'keep their identities', and (ii) various kinds of elaborate polarization patterns in a chain can be created by assembling the appropriate monomer types. In this respect, a [–$[CH_2–CF_2]$–$[CHF–CHF]$–]$_n$ system will be particularly interesting, with VDF units having large D_3 and [–CHF–CHF–] units large D_1 projections. Of course, such a level of precise monomer manipulation has not yet been achieved, but it may become possible in the future.

After understanding the behaviour of monomer structural units in isolated chains, we investigate the 'structural assembly' of chains. Starting from an isolated infinite chain, we gradually bring the chains together until a crystal is formed.

We computed the average VDF dipole moments for a system containing four β-PVDF chain segments of four units each in a pseudo-hexagonal arrangement in an orthorhombic supercell. The lattice constant c in the backbone direction was fixed at 2.56 Å/unit, while the lattice constants a and b were allowed to vary. Two calculations were carried out for each particular interchain distance (i.e. a combination of a and b). In the unrelaxed case, the ions were held fixed (in the same arrangement as for the relaxed isolated chain), so that only the electronic degrees of freedom were allowed to vary. In the relaxed-chains case, both the electrons and the ions were allowed to relax to their minimum energy positions. The ionic forces in the relaxed configuration were smaller than $0.025\,\text{eV}\,\text{Å}^{-1}$. The polarization of the crystalline structure was computed at the experimental lattice constants of $a = 8.58$ Å, $b = 4.91$ Å (polarization direction) and $c = 2.56$ Å (backbone direction) for the primitive orthorhombic cell with two structural units. The actual supercell used in the calculations for the crystal contained $1\times2\times4$ primitive cells.

The results of the calculations are presented in figure 4, where the average VDF dipole moments are plotted versus the interchain distance. The most striking feature of these curves is a dramatic increase in the VDF dipole moment as the chains are brought out from the noninteracting limit and assemble into the crystalline β-PVDF structure.

Apart from the fact that the 'collective polarization' enhancement in the β-PVDF crystal is much stronger than that in the isolated chain, the polarization curves of figure 4 show why many empirical models give polarization in β-PVDF that is too low.

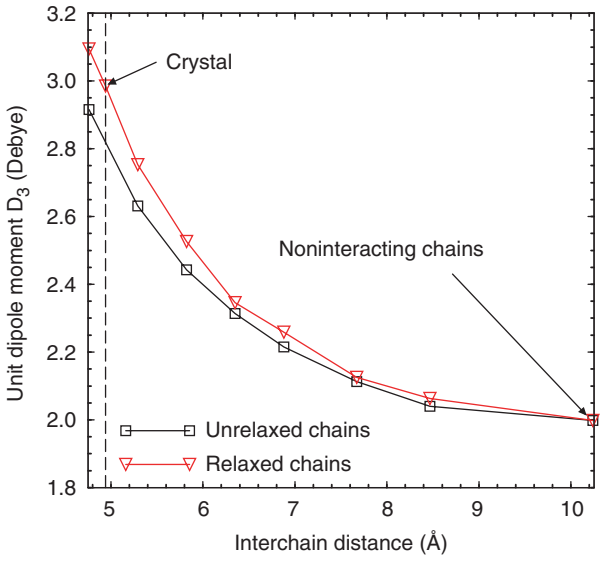

Figure 4. Average D_3 component of the VDF unit dipole moment in an infinite β-PVDF chain as the chains are brought together to form a crystal. See text.

Apparently, using the value of the VDF dipole moment of an isolated chain *in a crystal* (which is tempting since the former is well known) completely neglects the 'collective polarization' enhancement effect. *Ab initio* calculations unequivocally show that this effect is very large and has to be accounted for in order to get an accurate value for polarization in a fully crystalline β-PVDF. However, in addition to simply computing the magnitude of the polarization enhancement, our approach allows for an effective decoupling of the electronic and ionic contributions to it. If we compare the curves for the unrelaxed and relaxed chains in figure 4, we notice that even in the former case, i.e. with ions pinned in place, we still obtain 80% of the total polarization enhancement effect, indicating that the nature of the polarization increase is mostly electronic. Indeed, the calculations show that ionic relaxations only lead to an aproximately 1° narrowing of the F–C–F angle in a VDF monomer, leaving all of the bond lengths practically unchanged. On the other hand, the centres of WFs that are attached to a monomer's C–F and C–H bonds shift by 1–3%. The magnitudes of these shifts are on the order of 0.1 bohr, which is very small, but sufficient to produce the observed dipole-moment change of about 1 Debye.

Starting from the β-PVDF crystal we substituted some of the VDF units by TrFE and TeFE to create realistic models of P(VDF/copolymer) crystalline systems and to study their structural and polar properties. Since TrFE and TeFE structural units contain more 'bulky' fluorine atoms than VDF, simultaneous relaxations of the cells and ionic positions in the P(VDF/copolymer) systems are required.

In these calculations, one to eight units in the initial β-PVDF crystal were changed into TrFE or TeFE, which corresponds to copolymer concentrations of 6.25–50%. Each P(VDF/copolymer) structure was relaxed to stresses of less than 0.5 kbar and ionic forces of less than 0.025 eV $Å^{-1}$.

We find that there is no expansion along the direction of the carbon backbone—the only 'rigid' direction in the system—and only a weak expansion in the polarization direction in both families of models. This leaves the bulk of volume expansion to occur through the increasing lattice constant *a*. For the 50/50% VDF-to-copolymer concentration, in P(VDF/TrFE) and P(VDF/TeFE) systems *a* grows by 4.6 and 12.8%, respectively. For β-PVDF our calculations produce dihedral angles that are very close to 180°, which means that neighbouring units on a chain are all perfectly aligned in the polar direction. However, as the copolymer concentration grows, the monomers tend to tilt with respect to each other. This happens quickly in P(VDF/TrFE) and more gradually in P(VDF/TeFE), with dihedral angles dropping down to 170–172° at 50/50% VDF-to-copolymer ratio. The tilting process results in a less compact monomer arrangement in a chain (i.e. fluorine atoms 'stick out' more), translating into an increase in *a* lattice constant.

Turning to the polar properties of P(VDF/copolymer) crystalline models, we computed copolymer concentration-related changes in the dipole moment of every type of monomer (VDF, TrFE or TeFE) in each model family. The results are shown in figure 5, with the limiting values for monomer dipole moments in isolated infinite chains included for comparison. Clearly, the VDF dipole moment decreases in both P(VDF/TrFE) and P(VDF/TeFE) with growing copolymer concentration. However, even at 50/50% VDF-to-copolymer ratio, the VDF unit dipole moments are still approximately 20% larger than those in an isolated β-PVDF chain. The TrFE and TeFE monomer dipole moments in P(VDF/copolymer) crystals demonstrate a strongly nonlinear behaviour with respect to copolymer concentration. At TrFE concentration of less than 20%, TrFE unit in a crystal is more than twice as polar as in an isolated chain. At 50/50% VDF-to-TrFE concentration, it is still 40% more polar than that of an isolated chain. Analogously, in a crystal with TeFE concentration of less than 20%, this naturally nonpolar monomer has a dipole moment of 0.6–0.7 Debye and it stays polar even at 50/50% VDF-to-TeFE concentration.

Finally, in figure 6 we present the copolymer concentration dependence for the total polarization of the crystalline P(VDF/TrFE) and P(VDF/TeFE) models. The curves for both families closely follow the behaviour of VDF dipole moments in figure 5,

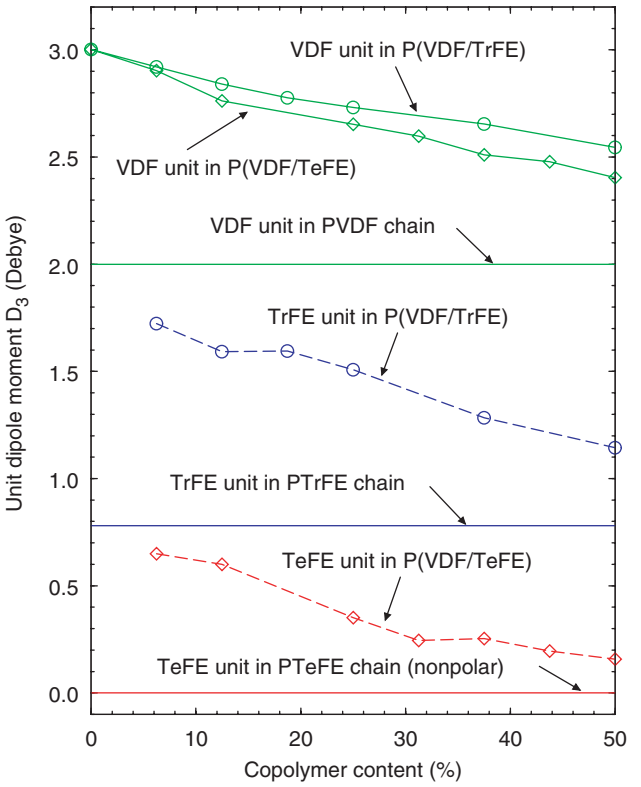

Figure 5. Changes in the values of average dipole moments of VDF, TrFE and TeFE structural units in the crystalline P(VDF/TrFE) and P(VDF/TeFE) models with increasing copolymer concentration. The limiting values of unit dipole moments in the isolated infinite β-PVDF, PTrFE and PTeFE chains are shown for comparison.

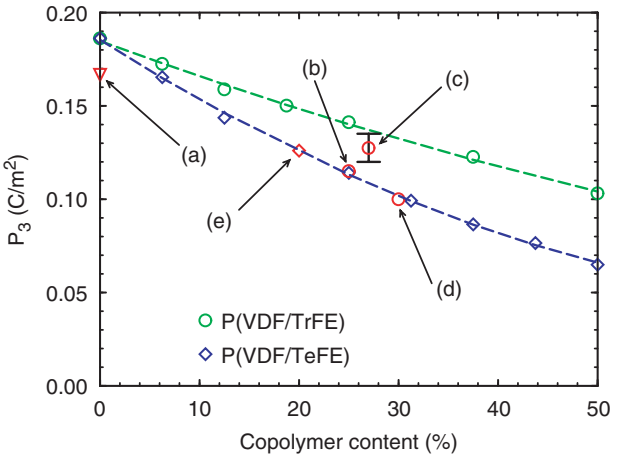

Figure 6. Changes in total polarization in the crystalline P(VDF/TrFE) and P(VDF/TeFE) models with increasing copolymer concentration. The dashed lines represent the fitted curves of equations (1). Extrapolations of experimental polarizations to 100% crystallinity are shown for comparison: (a) β-PVDF film of [46], (b) polycrystalline 75/25% P(VDF/TrFE) film of [18, 47], (c) 73/27% P(VDF/TrFE) sample of [16], (d) 70/30% P(VDF/TrFE) film of [48], (e) 80/20% P(VDF/TeFE) sample of [17]. See text for discussion.

displaying a similar downward bowing, which is a bit more pronounced in the case of P(VDF/TeFE). A fit to the curves provides an estimate of polarization (in C m^{-2}) at any copolymer fraction x in the range between 0 and 0.5:

$$P_3^{\mathrm{TrFE}}(x) = 0.185 - 0.20x + 0.069x^2,$$
$$P_3^{\mathrm{TeFE}}(x) = 0.185 - 0.34x + 0.201x^2. \qquad (1\,\mathrm{a})$$

A number of experimental observations, representing the polarization extrapolations to perfect crystallinity in β-PVDF, P(VDF/TrFE) and P(VDF/TeFE) are shown in figure 6 for comparison. This extrapolation is justified under the assumption that the dipoles in the noncrystalline part are randomly oriented, with zero net polarization. Point (a) refers to the polarization in the β-PVDF film of [46] linearly extrapolated from 60% crystallinity. The extrapolated value of polarization in the film (0.167 C m^{-2}) is approximately 10% lower than the one obtained in our calculations. Point (b) refers to the 100% polycrystalline 75/25% P(VDF/TrFE) film of [18, 47]. No correction was made for the variation of polarization direction among the crystalline grains. Point (c) refers to the polarization of 30–85% crystalline samples of 73/27% P(VDF/TrFE) extrapolated to 100% crystallinity by Tajitsu *et al.* [16], who estimated the polarization of a fully crystalline sample to be 0.120–0.135 C m^{-2}. Point (d) refers to a highly crystalline 70/30% P(VDF/TrFE) Langmuir–Blodget (LB) ultra-thin film of [48]. No extrapolation was made here because the crystallinity of the sample is not known. Of these three points, (c) exhibits the best agreement with the calculations. Equation (1a) estimates the polarization in 73/27% P(VDF/TrFE) to be 0.136 C m^{-2}, which is almost within the error bar of the experimental extrapolation. Comparing with the points (b) and (d), the computed polarizations are higher by 22% and 30%, respectively. The latter large discrepancy is most probably due to the fact that the 68 nm thin LB film has not yet reached bulk-like polarization. Finally, point (e) refers to the polarization obtained in 43–80% crystalline 80/20% P(VDF/TeFE) samples that were extrapolated to perfect crystallinity in [17]. This point shows an excellent agreement with the calculated polarization. In general, considering that our models represent ideal crystalline systems with no defects and ferroelectric domains, figure 6 demonstrates that our computations give an accurate upper-bound estimate of polarization in highly crystalline P(VDF/TrFE) and P(VDF/TeFE) structures through a wide range of copolymer concentrations, and that they can be

used as a guide to grow β-PVDF-type crystalline materials with predetermined polar properties.

Summarizing the dielectric materials part, we used the Wannier function formalism of the modern theory of polarization to carry out a comprehensive investigation of polar properties of β-PVDF-type chains and crystalline structures. It was explicitly demonstrated that the polarization strengths of VDF and copolymer monomers dramatically depend on their environment. This 'collective polarization enhancement' varies from almost zero in a chain to 50% in a crystal. The latter fact explains why many earlier models of β-PVDF, which were fitted to a sum of bond dipole moments of an isolated VDF unit, underestimate the polar properties of bulk polymers. We also studied the effects of weakly polar TrFE and nonpolar TeFE monomers in β-PVDF crystals, mapping out the evolution of the P(VDF/ copolymer) structural and polar properties through a wide range of experimentally useful copolymer concentrations. Analogously to β-PVDF, these structures exhibit strong 'collective polarization' enhancement, which has a weakly parabolic dependence on the copolymer concentration.

5. Many-body effects in optical absorption of water

The optical spectra of water, crystalline ice and amorphous ice are quite similar, so we opted to investigate naturally occurring hexagonal ice (ice-Ih) as a model system. The oxygen atoms in the ice-Ih structure lie on a hexagonal wurtzite lattice. Hydrogen atoms occupy the sites between neighbouring oxygens in a disordered fashion but subject to the ice rules, i.e. each oxygen is covalently bonded to two hydrogen atoms with the constraint that only one H atom can lie between two neighbouring O atoms. We model the disorder within a periodically repeated supercell consisting of 16 molecules [49].

In figure 7 we compare the optical spectra calculated according to these three levels of theory with experiment [20]. The spectrum obtained within DFT-GGA agrees with earlier independent-particle results [28]. The calculated onset of absorption occurs at too low energies (below 6 eV), and the first absorption maximum at about 8 eV is far less pronounced than the corresponding feature in experiment. The inclusion of the many-body electron–electron interaction in GWA, i.e. the electronic self-energy, leads to a nearly rigid blueshift of the spectrum, severely overestimating the energy positions of the measured peaks. The Coulomb correlation of electrons and holes, accounted for by solving the BSE, leads to the appearance of a sharp excitonic peak below the onset of the vertical quasiparticle transition energies. The peak positions and the line shape obtained from the BSE agree well with experiment. Since no input parameters to the calculation have been taken from experiment or fitted, the agreement between theory and measurement is truly impressive.

After having reproduced the main features of the optical absorption of ice, we explore the origin of the prominent first peak. To this end we calculate the optical transitions of gas-phase H_2O molecules. The GWA/BSE calculations are performed as for the solid, but the frequency-dependent inverse dielectric matrix is now computed in the independent-particle approximation. At the single-particle level of theory, i.e. in DFT-GGA, an energy of 6.2 eV is obtained for the lowest singlet pair excitation. The electronic self-energy blueshifts this value by 6.3 eV to 12.5 eV. This is partially compensated by an exciton binding energy of 5.3 eV, leading finally to an optical absorption at 7.2 eV, in excellent agreement with the experimental value of 7.4 eV [24]. These results can be compared with those for ice, shown in figure 7, where we find for the first absorption peak a self-energy shift of about 4.5 eV and an exciton binding energy (related to the position of the first major peak of the vertical optical transitions) of 3.2 eV. Self-energy and excitonic effects in ice are thus reduced by 29 and 40%, respectively, compared to gas-phase molecules. The reduction of the self-energy and the exciton binding energy upon condensation of the molecules is expected, due to the larger screening in the solid. The fact, however, that the exciton binding energy is more affected than the self-energy points to an

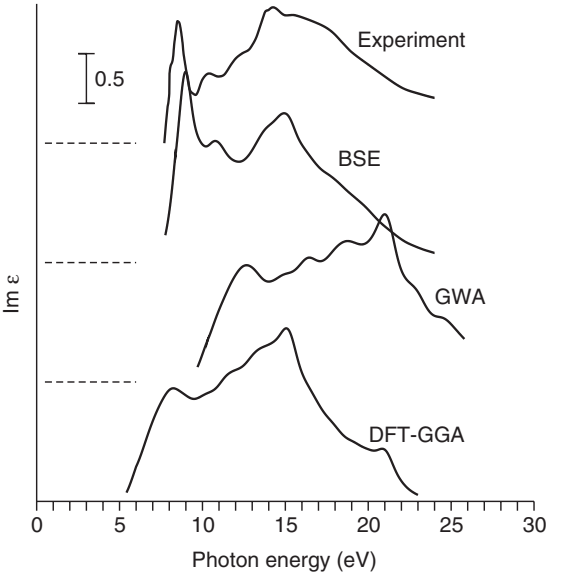

Figure 7. Imaginary part of the dielectric function of hexagonal ice measured at 80 K (from [20]), and calculated within the DFT-GGA, the GWA and from the BSE.

additional effect, namely a change in the localization of the exciton. The attractive interaction between an electron and a hole is inversely proportional to their average distance, the so-called exciton radius

$$R = \int d\mathbf{r}_e \int d\mathbf{r}_h |\mathbf{r}_e - \mathbf{r}_h| |\Psi(\mathbf{r}_e, \mathbf{r}_h)|^2, \qquad (1b)$$

where $\Psi(\mathbf{r}_e, \mathbf{r}_h)$ is the electron–hole pair wavefunction depending on the positions $\mathbf{r}_e$ and $\mathbf{r}_h$ of electrons and holes, respectively. The spatial distribution of electron–hole pairs therefore influences their energy.

In the case of an isolated molecule the localization of the electron–hole pair is immediately obtained from the spatial extension of the respective molecular orbitals, which relax upon optical excitation. The HOMO of water is a nonbonding oxygen-localized $1b_1$ orbital. It barely changes upon excitation of one electron into the LUMO. The latter, however, is strongly affected by partial occupation. The LUMO shows a significant probability density in the proximity of the O atom, as well as two lobes that protrude from the molecule in the proton directions, see figure 8(a). Optical excitation of one electron from the HOMO into the LUMO leads to a considerable expansion of these lobes, as shown in figure 8(b). Nevertheless, due to the attractive interaction with the hole at the oxygen atom, the electron remains close to the molecule. We calculate an average electron–hole distance R of 2.27 Å.

How does the spatial distribution of the excited electrons change upon condensation of the H_2O molecules? The solution of the BSE yields correlated electron–hole pair states. The pair wave functions $\Psi(\mathbf{r}_e, \mathbf{r}_h)$ are scalar functions in the two-particle space. The centre of gravity of the hole belonging to the exciton wave function responsible for the first absorption peak is close to an oxygen position τ_{oxygen}. In figure 9 we show the probability density $|\Psi(\mathbf{r}_e, \mathbf{r}_h = \tau_{oxygen})|^2$ corresponding to the electron distribution of that particular exciton. It is still reminiscent of the molecular LUMO shown in figure 8, but it expanded considerably farther towards the nearest-neighbour molecules. The calculated mean distance R between the electron and the hole is 4.02 Å, much larger than in the case of a gas-phase water molecule.

This finding provides an intuitive explanation for the surprising energy shift discovered in experiments: the matrix of surrounding H_2O molecules enables the optically excited electron to move farther away from the hole left behind at the oxygen atom, thus reducing the binding energy of the electron–hole pair from 5.3 to 3.2 eV. This effect overcompensates the narrowing of the HOMO–LUMO energy gap resulting from the condensation of the H_2O molecules and leads to the observed blueshift of the optical absorption. The sensitivity of the molecular exciton to hydrogen-bonded neighbour molecules suggests its possible modification by foreign molecules or ions in water solvent. More generally, the calculations show that the optically excited states of water molecules respond far more

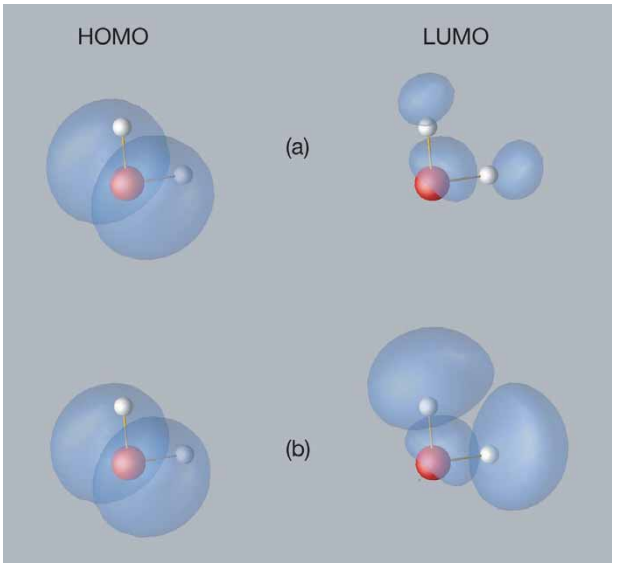

Figure 8. HOMO and LUMO of the gas-phase water molecule (a) in the ground state and (b) upon optical excitation.

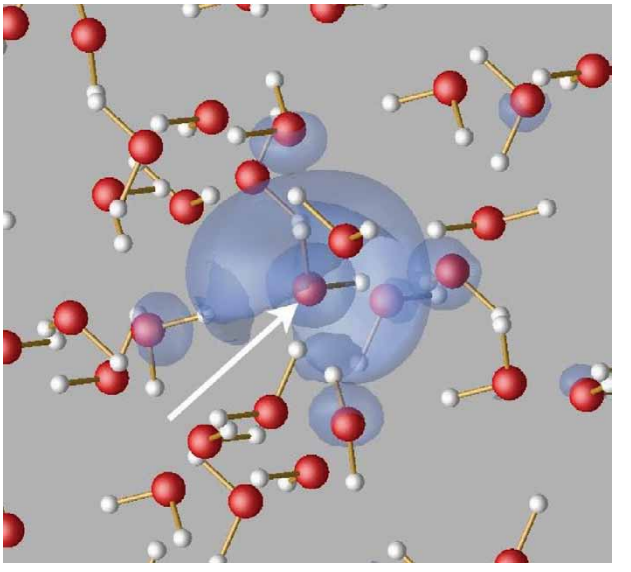

Figure 9. Spatial distribution of the electron in the exciton associated with the lowest optical absorption peak of ice-Ih. The hole is located at the oxygen position marked with an arrow (see text).

sensitively to intermolecular interactions than the ground state of their electronic structure.

References

[1] N. P. Guisinger, M. E. Greene, R. Basu, A. S. Baluch, and M. C. Hersam, Nano. Lett. **4,** 55 (2004).
[2] N. P. Guisinger, R. Basu, A. S. Baluch, and M. C. Hersam, Nanotechnology **15,** S452 (2004).
[3] T. Rakshit, G. C. Liang, A. W. Ghosh, and S. Datta, Nano. Lett. **4,** 1803 (2004).
[4] R. J. Hamers, J. S. Hovis, S. Lee, H. Liu, and J. Shan, J. Phys. Chem. B **101,** 1489 (1997).
[5] P. T. Hurley, A. E. Ribbe, and J. M. Buriak, J. Am. Chem. Soc. **125,** 11334 (2003).
[6] W. C. Lu, W. G. Schmidt, and J. Bernholc, Phys. Rev. B **68,** 115327 (2003).
[7] J. Cho and L. Kleinman, Phys. Rev. B **64,** 235420 (2001).
[8] Z. Liu, A. A. Yasseri, J. S. Lindsey, and D. F. Bocian, Science **302,** 1543 (2003).
[9] A. J. Lovinger, Science **220,** 1115 (1983).
[10] T. Furukawa, IEEE Trans. Electr. Insul. **24,** 375 (1989).
[11] R. G. Kepler and R. A. Anderson, Adv. Phys. **41,** 1 (1992).
[12] H. S. Nalwa (Ed.), *Ferroelectric Polymers* (Dekker, New York, 1995).
[13] G. Eberle, H. Schmidt and W. Eisenmenger, IEEE Trans. Diel. Electr. Insul. **3,** 624 (1996).
[14] G. A. Samara, Solid State Phys. **56,** 239 (2001).
[15] S. M. Nakhmanson, M. Buongiorno Nardelli and J. Bernholc, Phys. Rev. Lett. **92,** 115504 (2004).
[16] Y. Tajitsu, H. Ogura, A. Chiba, and T. Furukawa, Jpn. J. Appl. Phys. **26,** 554 (1987).
[17] S. Tasaka and S. Miyata, J. Appl. Phys. **57,** 906 (1985).
[18] K. Omote, H. Ohigashi, and K. Koga, J. Appl. Phys. **81,** 2760 (1997).
[19] R. Onaka and T. Takahashi, J. Phys. Soc. Jpn. **24,** 548 (1968).
[20] K. Kobayashi, J. Phys. Chem. **87,** 4317 (1983).
[21] G. D. Kerr, *et al*., Phys. Rev. A **5,** 2523 (1972).
[22] H. Hayashi, N. Watanabe, Y. Udagawa, and C.-C. Kao, Proc. Natl. Acad. Sci. USA **97,** 6264 (2000).
[23] V. F. Petrenko and I.A. Ryzhkin, Phys. Rev. Lett. **71,** 2626 (1993).
[24] W. F. Chan, G. Cooper, and C. E. Brion, Chem. Phys. **178,** 387 (1993).
[25] K. Laasonen, M. Sprik, M. Parrinello, and R. Car, J. Chem. Phys. **99,** 9080 (1993).
[26] G. P. Parravicini and L. Resca, Phys. Rev. B **8,** 3009 (1973).
[27] L. Resca and R. Resta, Phys. Status Solidi (b) **81,** 129 (1977).
[28] W. Y. Ching, M.-Z. Huang, and Y.-N. Xu, Phys. Rev. Lett. **71,** 2840 (1993).
[29] B. D. Bursulaya, J. Jeon, C.-N. Yang, and H. J. Kim, J. Phys. Chem. A **104,** 45 (2000).
[30] G. Onida, L. Reining, and A. Rubio, Rev. Mod. Phys. **74,** 601 (2002).
[31] E. L. Briggs, D. J. Sullivan, and J. Bernholc, Phys. Rev. B **54,** 14362 (1996).
[32] B. Larade, J. Taylor, H. Mehrez, and H. Guo, Phys. Rev. B **64,** 075420 (2001).
[33] M. Brandbyge, J. L. Mozos, P. Ordejon, J. Taylor, and K. Stokbro, Phys. Rev. B **65,** 165401 (2002).
[34] J. L. Fattebert and J. Bernholc, Phys. Rev. B **62,** 1713 (2000).
[35] M. Buongiorno Nardelli, J.-L. Fattebert, and J. Bernholc, Phys. Rev. B **64,** 245423 (2001).
[36] R. D. King-Smith and D. Vanderbilt, Phys. Rev. B **47,** 1651 (1993); D. Vanderbilt and R. D. King-Smith, *ibid*. **48,** 4442 (1993).
[37] R. Resta, Rev. Mod. Phys. **66,** 899 (1994).
[38] M. S. Hybertsen and S. G. Louie, Phys. Rev. B **34,** 5390 (1986).
[39] S. Albrecht, L. Reining, R. Del Sole, and G. Onida, Phys. Rev. Lett. **80,** 4510 (1998).
[40] L. X. Benedict, E. L. Shirley, and R. B. Bohn, Phys. Rev. Lett. **80,** 4514 (1998).
[41] M. Rohlfing and S. G. Louie, Phys. Rev. Lett. **83,** 856 (1999).
[42] L. J. Sham and T. M. Rice, Phys. Rev. **144,** 708 (1966).
[43] W. Hanke and L. J. Sham, Phys. Rev. B **12,** 4501 (1975); *ibid*. **21,** 4656 (1980).
[44] P. H. Hahn, W. G. Schmidt, K. Seino, M. Preuss, F. Bechstedt, and J. Bernholc, Phys. Rev. Lett. **94,** 037404 (2005).
[45] H. M. G. Correia and M. M. D. Ramos, Comput. Mater. Sci. **33,** 224 (2005).
[46] To the best of our knowledge, the most recent synthesis techniques produce films with crystallinity of about 60%. See K. Nakamura, D. Sawai, Y. Watanabe, D. Taguchi, Y. Takahashi, T. Furukawa, and T. Kanamoto, J. Polym. Sci. Part B **41,** 1701 (2003).
[47] H. Ohigashi, K. Omote, and T. Gomyo, Appl. Phys. Lett. **66,** 3281 (1995).
[48] H. Kliem and R. Tadros-Morgane, J. Phys. D: Appl. Phys. **38,** 1860 (2005).
[49] I. Morrison, *et al*., J. Phys. Chem. B **101,** 6146 (1997).